PNAS RESEARCH ARTICLE | CELL BIOLOGY OPEN ACCESS

In situ structural analysis reveals membrane shape transitions during autophagosome formation

Anna Bieber[a,b,c,1], Cristina Capitanio[b,c,1], Philipp S. Erdmann[a,d,2], Fabian Fiedler[e], Florian Beck[a,f], Chia-Wei Lee[a,g], Delong Li[e], Gerhard Hummer[c,h,i], Brenda A. Schulman[b,c,2], Wolfgang Baumeister[a,c,2], and Florian Wilfling[a,b,c,e,2]

Contributed by Wolfgang Baumeister; received June 10, 2022; accepted August 9, 2022; reviewed by Aaron Ciechanover and Alexander Varshavsky

Autophagosomes are unique organelles that form de novo as double-membrane vesicles engulfing cytosolic material for destruction. Their biogenesis involves membrane transformations of distinctly shaped intermediates whose ultrastructure is poorly understood. Here, we combine cell biology, correlative cryo-electron tomography (cryo-ET), and extensive data analysis to reveal the step-by-step structural progression of autophagosome biogenesis at high resolution directly within yeast cells. The analysis uncovers an unexpectedly thin intermembrane distance that is dilated at the phagophore rim. Mapping of individual autophagic structures onto a timeline based on geometric features reveals a dynamical change of membrane shape and curvature in growing phagophores. Moreover, our tomograms show the organelle interactome of growing autophagosomes, highlighting a polar organization of contact sites between the phagophore and organelles, such as the vacuole and the endoplasmic reticulum (ER). Collectively, these findings have important implications for the contribution of different membrane sources during autophagy and for the forces shaping and driving phagophores toward closure without a templating cargo.

autophagy | cryo-electron tomography | autophagosome biogenesis | organelle contact sites | membrane structure

Significance

Macroautophagy is a degradation process fundamental for (eukaryotic) cellular homeostasis, in which cytosolic material is engulfed by a double-membrane autophagosome for delivery to a lytic compartment. In this study, we capture transient intermediates of autophagosome biogenesis within yeast cells at previously unattained resolution by correlative cryo-electron tomography (cryo-ET). Our quantitative analysis of autophagic membranes reveals unexpected structural features and shape transitions from open phagophores to closed autophagosomes. We further define the subcellular environment of autophagic structures, uncovering polarized contact sites with specific organelles. These results have direct implications for the membrane sources in autophagy and for the forces inducing phagophore shape, thus highlighting the potential of cryo-ET at the junction of biophysics and cell biology.

Macroautophagy (autophagy hereafter) is a key pathway to maintain cellular homeostasis. In this process, a de novo synthesized double-membrane vesicle, the autophagosome, engulfs cellular material in response to stress conditions (1). This culminates in autophagosome fusion with lysosomes (or the vacuole in yeast) to remove and recycle its cargo. Fluorescence microscopy has identified the hierarchical order of the autophagy machinery during autophagosome biogenesis (2, 3). In addition, many of the membrane intermediates have been visualized at low resolution with conventional electron microscopy (4–7). These and other methods have revealed that autophagy proceeds in several steps: (I) membrane nucleation, (II) growth of the cup-shaped phagophore, (III) closure, and (IV) fusion of the autophagosome with the lytic compartment (8). Meanwhile, pioneering genetic and biochemical studies have revealed key regulators of autophagosome biogenesis (8, 9). In yeast, nitrogen starvation triggers the first step of phagophore nucleation through assembly of the molecular machinery in the pre-autophagosomal structure (PAS) next to the vacuole (10). The phagophore is initially formed by fusion of few vesicles carrying the transmembrane protein Atg9 (11–13). It then grows both by fusion of vesicles (e.g., Atg9 or COPII vesicles (14)) and by lipid transfer from the endoplasmic reticulum (ER) through protein complexes such as Atg2/Atg18 (15). Membrane expansion is further driven by conjugation of the ubiquitin-like protein Atg8 to phosphatidylethanolamine in the phagophore membrane (16). During growth, the initial membrane disk assumes a characteristic cup shape, a transition that is likely driven by the highly curved and therefore energetically unfavorable phagophore rim (17). After closure and maturation, the resulting autophagosome fuses with the vacuole, releasing the inner vesicle—now called "autophagic body"—for degradation.

Despite the importance of autophagy and the efforts in deciphering the molecular machinery underlying it (8), it is still unknown how membranes are organized and transformed on an ultrastructural level during autophagosome biogenesis. In situ cryo-electron tomography (cryo-ET) can reveal membrane structures directly in their native cellular environment (18, 19). Yet monitoring the formation of an organelle poses the challenge to capture a rare event with many intermediates along the process. To overcome these hurdles, we combined several strategies to dissect the formation of autophagosomes using cryo-ET: (I) stimulating their formation to increase the abundance of all species involved, (II) using mutants that accumulate intermediates that are naturally short lived, and (III) fluorescently labeling the autophagy machinery or its cargo to

[1]A.B. and C.C. contributed equally to this work.

[2]To whom correspondence may be addressed. Email: florian.wilfling@biophys.mpg.de, schulman@biochem.mpg.de, baumeist@biochem.mpg.de, or philipp.erdmann@fht.org.

This article contains supporting information online at http://www.pnas.org/lookup/suppl/doi:10.1073/pnas.2209823119/-/DCSupplemental

Published September 19, 2022.

specifically target those structures during focused ion beam (FIB) milling and tomogram acquisition.

Using this approach, we captured the major membrane structures in bulk autophagy within their native context and at high resolution. Our detailed data analysis provides important insights into the biophysics of autophagosome biogenesis. While we focus here on yeast autophagy, our study highlights the potential of correlative cryo-ET in analyzing short-lived cellular structures and provides a general template for studying the formation of organelles.

Results

Correlative Cryo-ET Resolves Different Steps of Autophagosome Biogenesis. We used nitrogen starvation to robustly induce autophagy in *Saccharomyces cerevisiae* cells (20, 21) and employed two alternative fluorescence labeling strategies: (I) overexpressing tagged Atg8 to mark autophagic structures, since Atg8 is conjugated to the phagophore membrane and is present in most stages of autophagy (16) (Fig. 1*A*), and (II) overexpressing the cargo protein eGFP-Ede1, either alone or in combination with mCherry-Atg8 (*SI Appendix*, Fig. S1 *A–E*). Ede1 overexpression leads to accumulation of endocytic machinery proteins at the plasma membrane in a compartment called END (Ede1-dependent endocytic protein deposits), a selective autophagy cargo (22). Thus, eGFP-Ede1 marks autophagic structures independent of Atg8 overexpression. The starved cells were subjected to a correlative FIB-milling and cryo-ET workflow (23, 24): after plunge freezing, cryo-fluorescence stacks were recorded. Fiducial-based three-dimensional (3D) correlation with FIB/scanning electron microscopy (SEM) and transmission electron microscopy (TEM) images targeted structures of interest during lamella milling and tilt-series acquisition (*SI Appendix*, Fig. S1 *A–E*). The correlation thus identifies and provides evidence for the autophagic nature of the structures in the tomograms (Fig. 1 *B–D*).

The captured key steps of autophagosome biogenesis (Fig. 1 *E–H*) include early phagophores, in which the membrane disk is slightly bent to form a small concave structure (Fig. 1 *E* and *I* and *SI Appendix*, Fig. S1*A*). Next, we frequently observed expanded, cup-shaped phagophores with a clearly visible opening to the cytoplasm (Fig. 1 *F* and *J* and *SI Appendix*, Fig. S1*B*). Furthermore, we found closed autophagosomes, for which no opening or rim is visible (Fig. 1 *G* and *K* and *SI Appendix*, Fig. S1*C*), and autophagic bodies, often still partially wrapped by the outer autophagosome membrane fused with the vacuole (Fig. 1 *H* and *L* and *SI Appendix*, Fig. S1*D*). Importantly, the autophagic structures correlated to the cargo eGFP-Ede1 are indistinguishable from the structures found in cells expressing only eGFP-Atg8 (*SI Appendix*, Fig. S1 *F–H*). In total, we collected 35 tomograms of open phagophores, as well as 17 structures without any visible opening. To capture more closed autophagosomes, we created an eGFP-Ede1 mutant strain lacking the Rab7-like guanosine triphosphatase Ypt7, resulting in accumulation of autophagosomes in the cytosol (25). This strain yielded additional 25 closed autophagosomes (and two phagophores) that closely resembled the ones obtained from the wild-type strain (*SI Appendix*, Fig. S1 *F, G*, and *I*).

Cargo Templating Is Not Essential for Autophagosome Formation under Bulk Conditions. During nutrient starvation, autophagic structures mainly engulf cytosolic ribosomes, as shown by earlier electron microscopy (EM) studies (5), but can still retain selectivity for specific cargo (26–29). In line with this, 98 out of 104 autophagic structures contained ribosomes alone or next to selective cargo like the END or the cytoplasm-to-vacuole targeting (30) cargo prApe1 (31) (Fig. 2 *A–C* and *SI Appendix*, Fig. S2*A*). Only in few cases, we observed the exclusive uptake of selective cargo (*SI Appendix*, Fig. S2 *B* and *C*). To test whether cytosolic cargo clusters to guide phagophore growth during nitrogen starvation, we extracted ribosome positions in the tomograms by template matching and subtomogram averaging (Fig. 2 *B* and *C* and *SI Appendix*, Fig. S2*E*). In five example tomograms, we found no difference between the density of ribosomes inside (cargo) and outside (cytosolic) of autophagic structures (*SI Appendix*, Fig. S2*F*). Next, we compared the nearest neighbor distances (NNDs) of cargo and cytosolic ribosomes in 77 tomograms. Also in this case, neither median nor mean NNDs were significantly different for cargo and cytosolic ribosomes (Fig. 2*D* and *SI Appendix*, Fig. S2*G*). This suggests that, under starvation conditions, autophagosomes mostly engulf cytosol nonspecifically and can form without any detectable cargo guiding the membrane.

Phagophores Show Distinct Contact Sites with Other Organelles. Phagophore contacts with other organelles like the ER or the vacuole are known to be crucial for autophagosome biogenesis (10, 32, 33). To systematically map the subcellular environment of autophagy, we measured the frequency and distance of organelles observed near autophagosomes and phagophores in the tomograms. Particularly the vacuole, ER, nuclear membrane, vesicles, and lipid droplets (LDs) were frequently found close to autophagic structures (often <100 nm, Fig. 3 *A* and *B*). To confirm these findings, we analyzed the colocalization of Atg8-positive structures with other organelles by fluorescence microscopy (Fig. 3*C*). In agreement with the EM analysis, Atg8 puncta were frequently found at the vacuole (63% of Atg8 puncta) and the ER (61%), specifically at ER exit sites (33) (47%). Unlike mitochondria (<10%), Atg8 puncta still colocalized with LDs in 30% of the cells (Fig. 3*C*).

To distinguish functional contact sites from random ones, we identified two ultrastructural features: first, open phagophores are distinctly polar, with the highly curved rim connecting the inner to the outer membrane. We reasoned that frequent contacts to a distinct part of the phagophore would be a strong indication of a functionally relevant interaction. Accordingly, we assigned each contact with a minimum distance of 100 nm or less to one of the categories "rim", "inside", "back", and "side", based on the area where the closest interaction was observed (Fig. 3*D* and *SI Appendix*, Fig. S3*A*). Second, in the absence of external forces, a phagophore is expected to adopt a cup-shape form, with the circular rim region as the only high-curvature area (17). Membrane deformations at contact sites could therefore indicate a specific interaction, as they imply additional forces. For quantification, we sorted them into four categories: (I) high-curvature peaks of the autophagic membrane toward another organelle, (II) extended contacts over a large area, (III) extensions of the phagophore rim toward the other organelle (*SI Appendix*, Fig. S3*B*), and (IV) global deformations of the whole structure toward the contact (Fig. 3*E*). Applying these features to the cryo-ET data, four organelles stand out: the vacuole, LDs, nuclear membrane, and ER.

The Back or Side of Growing Phagophores Is Anchored to the Vacuole. Even though the phagophore assembly site has long been known to localize to the vacuole (10), the tomograms reveal previously unreported aspects of this interaction (Figs. 3 and 4 *A* and *B*). First, open phagophores almost never interact

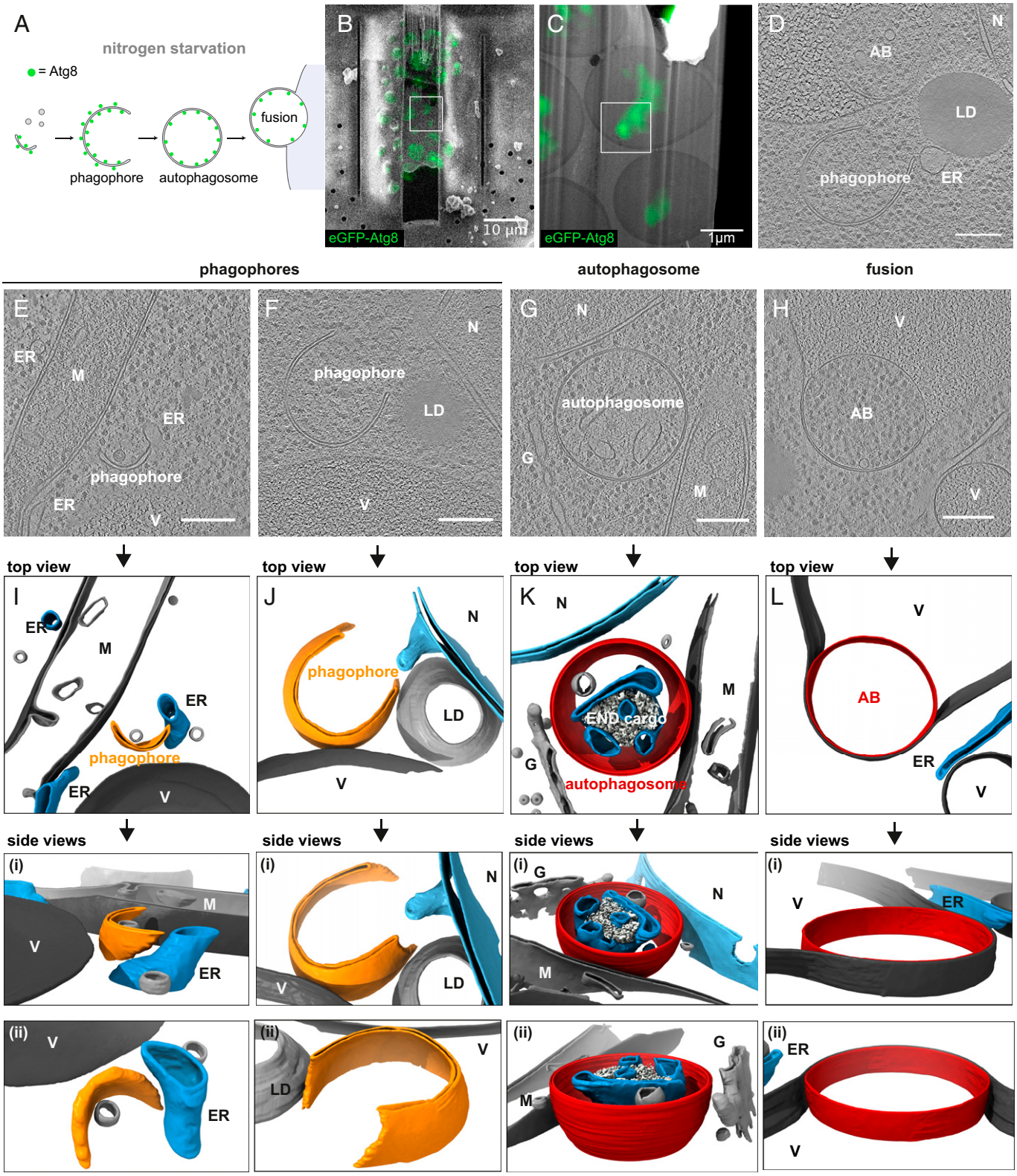

Fig. 1. Correlative cryo-ET captures key steps of autophagy in yeast. (*A*) Key autophagy intermediates can be targeted with eGFP-Atg8. (*B* and *C*) SEM and TEM overviews of a lamella, overlaid with correlated eGFP-Atg8 cryo-fluorescence signal (green) used to target the autophagic structures (white boxes). (*D*) Slice through a tomogram acquired in the boxed area in *C* reveals an autophagic body (AB) (*Top*) and an open phagophore (*Bottom*). (*E–H*) Exemplary tomogram slices and segmentations of key autophagy steps captured with correlative cryo-ET. All tomogram scale bars: 200 nm. (*I–L*) 3D renderings in top and zoomed-in side views (*i* and *ii*) of autophagic structures and organelles in the tomograms shown in *E–H*. N, nucleus, M, mitochondrion, V, vacuole, G, Golgi apparatus.

with the vacuole through the rim (Fig. 3*D*). This leads to a more frequent orientation of the phagophore opening parallel to or away from the vacuole (*SI Appendix*, Fig. S3*C*). Second, half of the phagophores within 100 nm of the vacuole exhibit deformations at the contact sites, with most structures either forming a peak ($n = 8$) or following the vacuole over an extended area ($n = 7$) (Figs. 3 *E* and 4 *A* and *B* and *SI Appendix*, Fig. S3 *D* and *E*). In contrast, closed autophagosomes show only

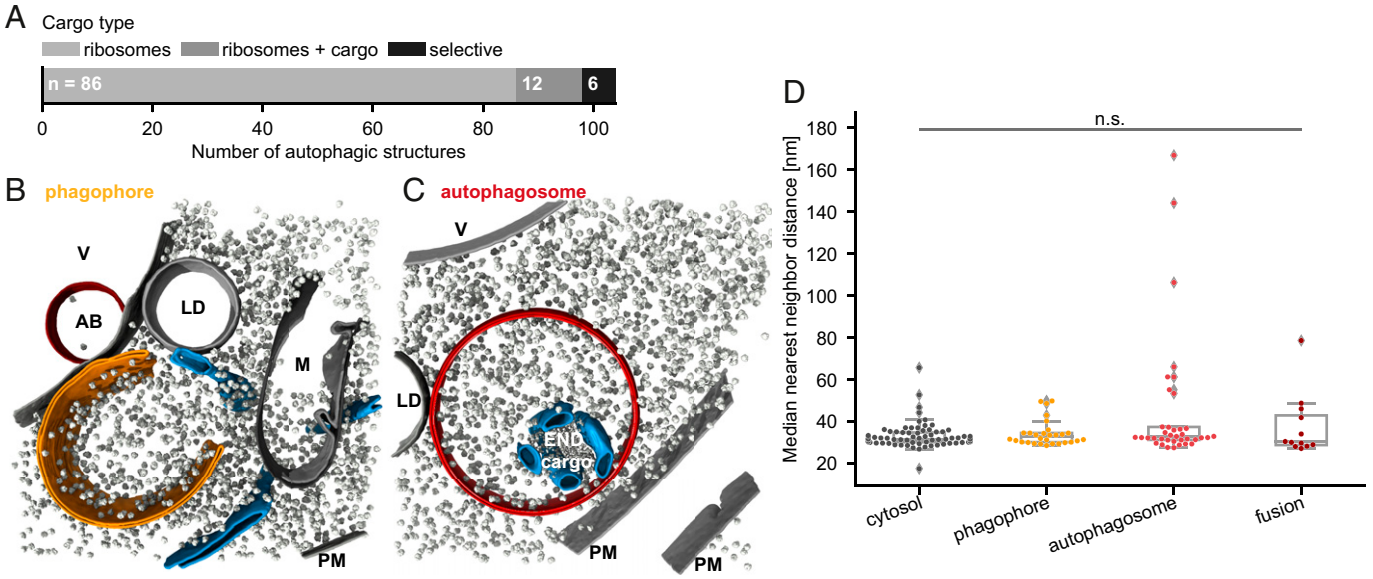

Fig. 2. Cargo templating is not essential for autophagosome formation under bulk autophagy conditions. (*A*) Numbers of captured autophagic structures containing only ribosomes, ribosomes and selective cargo, or exclusively selective cargo. (*B*) 3D rendering of an open phagophore (orange) in its native environment, surrounded by ribosomes (gray) and organelles (ER (blue), AB, LD = lipid droplet, M = mitochondrion, and PM = plasma membrane). (*C*) Segmentation of a closed autophagosome (red) containing ribosomes and the amorphous Ede1-dependent endocytic protein deposit (END) cargo, surrounded by ER (blue). (*D*) Comparison of ribosome nearest neighbor distances in different compartments. Each dot represents the median distance measured for one tomogram. Differences between cytosol and autophagic ribosome distances were analyzed with the Wilcoxon signed-rank test, treating values from compartments in the same tomogram as paired (n = 77 tomograms). n.s., not significant, $P \geq 0.05$.

two extended contacts and one peak in a total of 14 tomograms (Fig. 3*E*, only wild-type strains). This indicates that these distortions are a characteristic feature of growing phagophores anchored to the vacuole that is largely absent in mature autophagosomes.

A detailed analysis of the peak-shaped phagophore–vacuole contact sites reveals that they are highly heterogeneous, with peak heights ranging from 3.6 to 33 nm, peak widths from 16 to 32 nm (full width at half maximum), and the minimum distance to the vacuole from 19 to 53 nm (Fig. 4 *A*–*C*). The average Pearson's correlation coefficient between peak elevation and vacuole distance is −0.75, indicating that the phagophore membranes indeed extend toward the vacuole (*SI Appendix*, Table S1 and Fig. S3*F*). Extended phagophore–vacuole contacts are equally heterogeneous. Their minimum distances range from 4 to 20 nm and contact areas from 100 to 400 nm^2 (*SI Appendix*, Fig. S4*G*). Thus, apart from the preference for the phagophore side and back, there is no clear consensus structure of the contacts with the vacuole. The difference in phagophore–vacuole spacing also argues against a rigid spacer that would keep the membranes at a fixed distance. However, the local high-curvature areas and deformations in the open phagophores imply that they are physically tethered to the vacuole, withstanding forces strong enough to cause such drastic membrane deformations.

LDs Associate with Autophagic Structures and Deform Phagophores. LDs are necessary for starvation-induced autophagy in yeast, as their absence inhibits the formation of autophagic structures (34). LDs have been proposed to act as additional source of lipids for phagophore growth (35) and as regulators of autophagy by contributing to ER homeostasis as well as maintaining the phospholipid composition (36). Still, contact sites between LDs and autophagic structures remain largely unexplored (35). In the tomograms, LDs are found sometimes inside (*SI Appendix*, Fig. S2 *A* and *B*) and often next to both phagophores and autophagosomes (Figs. 3 *A* and 4 *D*) but do not have a preferred phagophore interaction region (Fig. 3*D*). However, membrane deformations at contacts are observed in two cases in which the phagophore rim clearly extends toward a LD (Figs. 3 *E* and 4*D*). While the phagophore–LD distance is rather large in the first case (60 nm, Fig. 3*E*), the rim gets very close to the LD in the second (12 nm, Figs. 3 *E* and 4 *D*), thereby suggesting a rare but functional contact.

The Phagophore Rim Is Tethered to the ER and the nuclear membrane. Fluorescence microscopy studies have shown a frequent colocalization of PAS and ER but also with the nuclear membrane (NM) (33) (Fig. 3*B*). This is consistent with the cryo-ET data, where tubular ER is observed within 100 nm of the phagophore in more than 50% of the cases (Fig. 3*D*). NM contacts are rarer, but both NM and ER contacts with the phagophore show a strong preference for the rim (Fig. 3*D*).

While no strong deformations of the phagophore are observed close to the ER (Figs. 3 *E* and 4 *E*), in all five cases in which the NM is within 100 nm of the phagophore, the contact happens through a deformation at the rim toward the nucleus (Figs. 3 *E* and 4 *F* and *SI Appendix*, Fig. S4*A*). Interestingly, phagophore–nucleus contacts cannot only deform the phagophore but also the NM (Fig. 4*F*), suggesting a strong physical connection between the two organelles. The absence of obvious membrane distortions at contact sites with tubular ER may be explained by its higher motility and lack of physical constraints.

The frequent observation of ER–rim contacts is consistent with their predicted role as lipid transfer sites for phagophore expansion (37). Recent studies provide strong evidence that lipids are shuttled from the ER to the phagophore through the Atg2/Atg18 complex (15), known to localize to the phagophore rim (3, 33). Based on the structure of its human homolog (38), Atg2 could span roughly 20 nm (39) and phagophores are observed within that distance of the ER or NM in 15 tomograms. In 10 of these sites that were analyzed in more detail, the ER contact area ranges from 320 to 14,500 nm^2, with a median of around 1,600 nm^2 (*SI Appendix*, Table S2). The ER

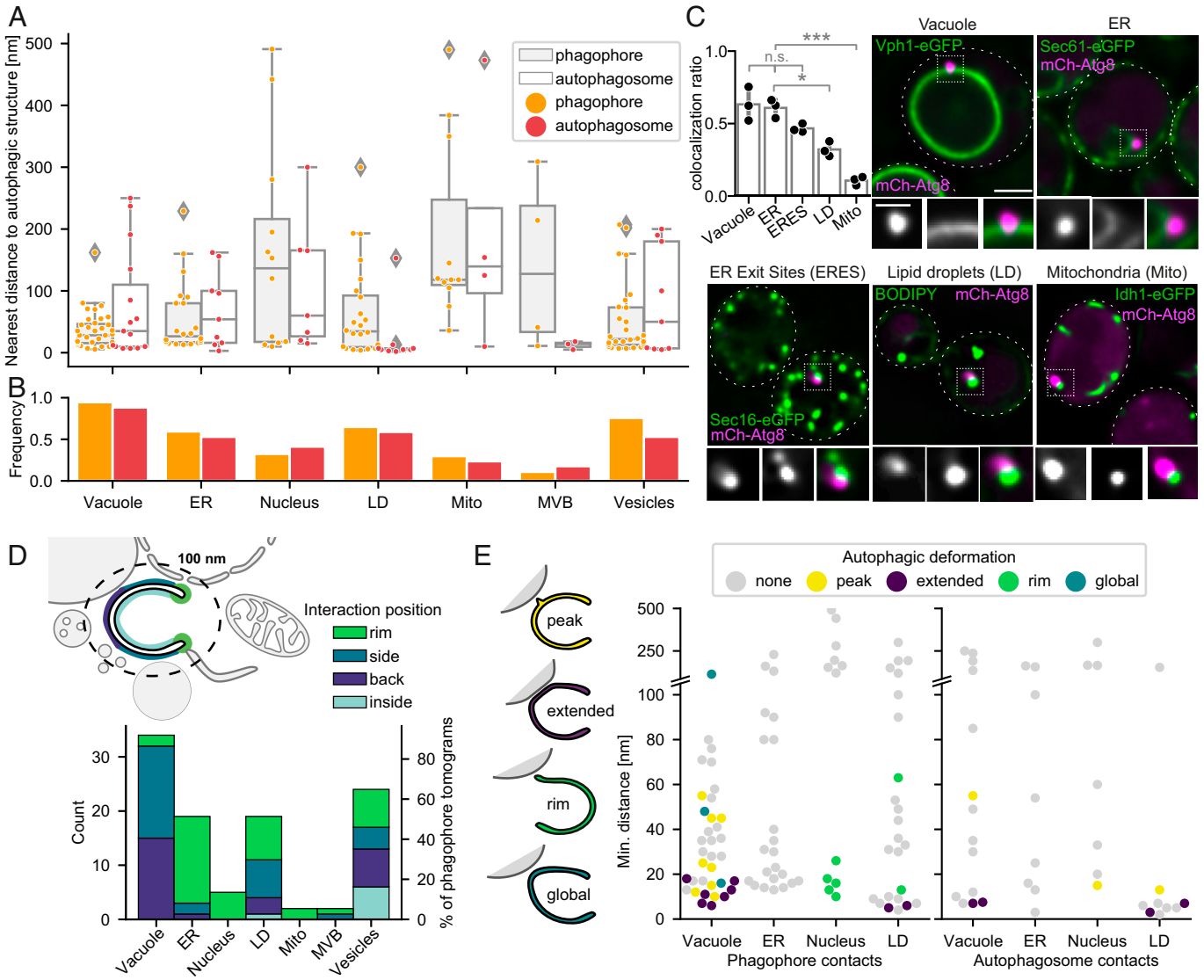

Fig. 3. Autophagic structures interact with other organelles. (*A*) Nearest distance of different organelles to phagophores (orange) or autophagosomes (red) measured in the tomograms. (*B*) Frequency at which different organelles are observed in tomograms of phagophores ($n = 35$) or autophagosomes ($n = 17$). (*C*) Quantification and examples of mCherry-Atg8 (mCh-Atg8) colocalization with different organelles. For each organelle, the colocalization ratio with Atg8 was measured in three replicates with >100 cells each. Statistical analysis: Kruskal–Wallis H test and pairwise Games–Howell post hoc test. ***$P < 0.001$, **$P < 0.01$, *$P < 0.05$, n.s., $P \geq 0.05$. Scale bar in large image, 2 μm, scale bar in small image, 1 μm. (*D*) Preferred contacts of organelles with different parts of the phagophore. Contact positions (rim, side, back, and inside) are quantified for organelles within 100 nm of the phagophore. (*E*) Deformations of autophagic structures at contact sites with other organelles, plotted against the minimum distance for phagophores (*Left*) and autophagosomes (*Right*). *Left*, schematic depictions of deformation categories; peaks (yellow), extended contacts (purple), rim deformations (green), and global deformations (petrol).

shows a local increase in curvature with decreasing distance to the phagophore in 4/10 tomograms (*SI Appendix*, Fig. S4*B*). In some cases, the phagophore rim and ER are clearly connected by densities with lengths of 17 ± 3 nm ($n = 11$, *SI Appendix*, Fig. S4*C*), which are, however, too heterogeneous and rare to be analyzed by subtomogram averaging. Still, we note that at all sites with such densities the local curvature of the phagophore membrane is higher than the local ER curvature (*SI Appendix*, Fig. S4*D*), which might have implications for lipid transfer.

In summary, phagophore–ER contacts almost exclusively happen through the rim and connect the phagophore to the ER or NM. The observed membrane deformations suggest a physical connection between the organelles. Based on the short distance and several clearly visible connecting densities, these contacts could function as Atg2-mediated lipid transfer sites.

Unique Structural Features of Autophagic Membranes. To gain detailed insights into the membrane transformations in autophagy, we first identified suitable parameters and developed methods to characterize autophagic structures with minimal manual intervention. Accordingly, membranes were segmented automatically to ensure objectivity of the results (40). The overall dimensions of the autophagic structures were then estimated from the ∼150-nm-thick lamella slices by fitting ellipsoids to the inner membranes, and a sphericity index (41) was calculated for each of the structures (Fig. 5 *A* and *B*). As estimated from the volumes of the best-fitting ellipsoids (Fig. 5*A*), phagophores and autophagosomes are overall similar in size. However, while closed autophagosomes are almost perfectly spherical, phagophores show significantly lower sphericity indices (Fig. 5*B* and *SI Appendix*, Fig. S5 *A* and *B*). This is consistent with the reported elongation of growing phagophores in mouse embryonic fibroblasts (17, 42).

A crucial parameter that determines the shape of autophagic structures is the distance between the inner and outer membrane. To quantify this intermembrane spacing, we developed a

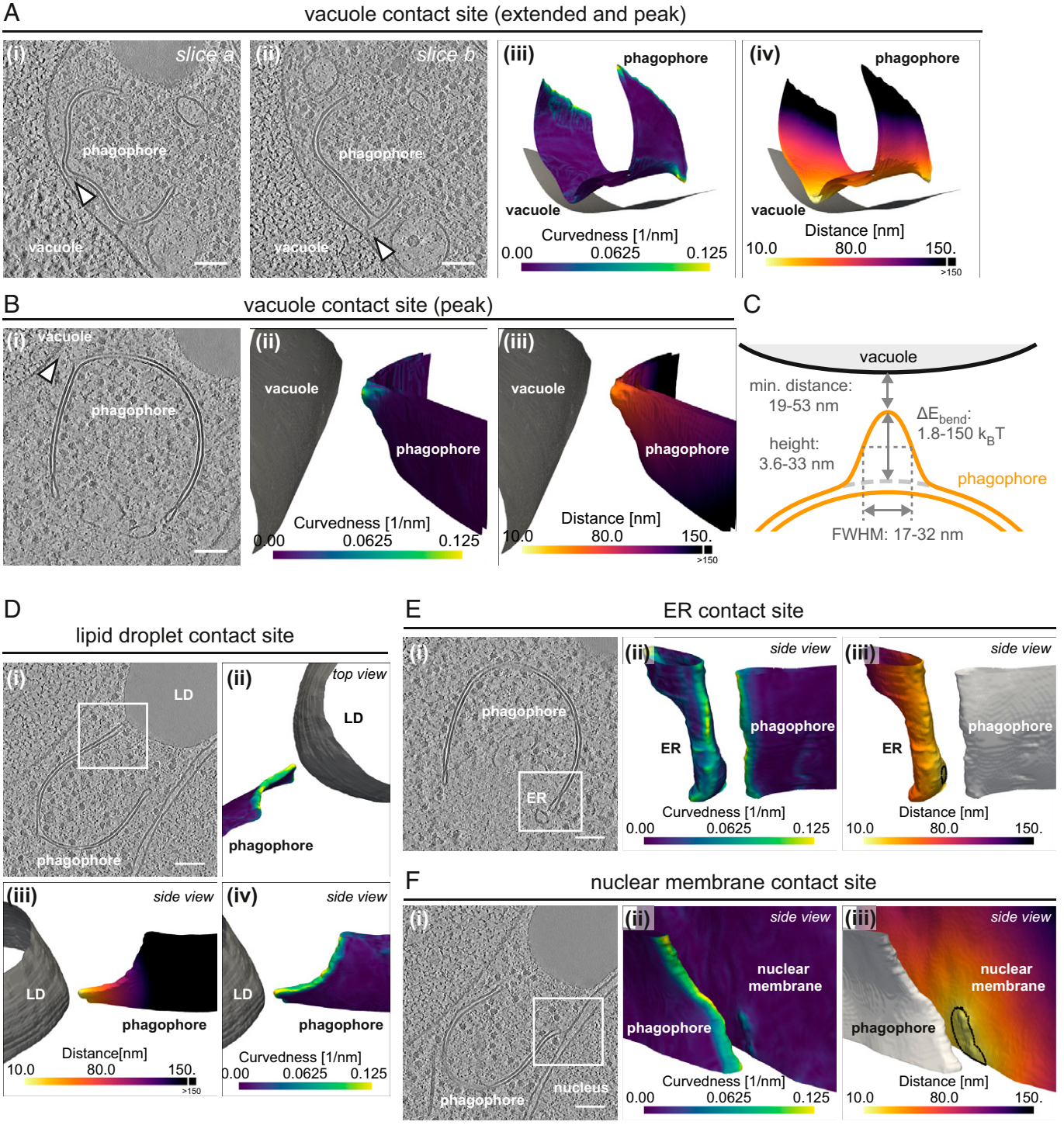

Fig. 4. Phagophores engage in specific contacts with the vacuole, LDs, ER, and nuclear membrane. (*A*) Phagophore with a peak and an extended vacuole contact site. (*i* and *ii*) Tomogram slices with arrowheads indicating the extended (*i*) and peak (*ii*) contact site. All scale bars 100 nm. (*iii* and *iv*) Membrane segmentations colored by local curvedness (*iii*) and distance to the vacuole (*iv*). (*B*) Peak-shaped deformation of the phagophore membrane toward the vacuole. Tomogram slice (*i*) and segmentations colored according to local curvedness (*ii*) and distance to the vacuole (*iii*). (*C*) Shape parameters (full range) of phagophore peaks toward the vacuole measured for seven peaks. (*D*) A rare example of a rim deformation toward a LD. Tomogram slice (*i*) and top and side views (*ii–iv*). (*E* and *F*) Phagophore contacts with the ER (*E*) and nuclear membrane (*F*). Tomogram slices (*i*) and membrane segmentations colored according to local curvedness (*ii*) and distance to the phagophore (*iii*). The black line on the segmentations marks the membrane areas close enough for Atg2 to bridge the distance.

robust minimum distance algorithm (*SI Appendix*, *SI Methods*), which can handle holes and overhangs in segmentations and measures the distance from thousands of points. Notably, the average intermembrane distance of autophagic structures is significantly smaller than in mitochondria, the NM, and ER sheets (Fig. 5*C*). The observed 9–11 nm spacing (measured from middle of one phospholipid bilayer to middle of the other bilayer) is also smaller than previously reported for autophagosomes (20–50 nm in general, <30 nm in yeast) (43). Both autophagosomes and their fusion intermediates display similar values (8.9 ± 0.79 nm and 8.5 ± 0.72 nm, mean ± SD, $n = 42$ and $n = 12$, respectively), which is strikingly homogenous across the whole membrane (Fig. 5*C*). This makes the intermembrane distance of autophagic structures a unique

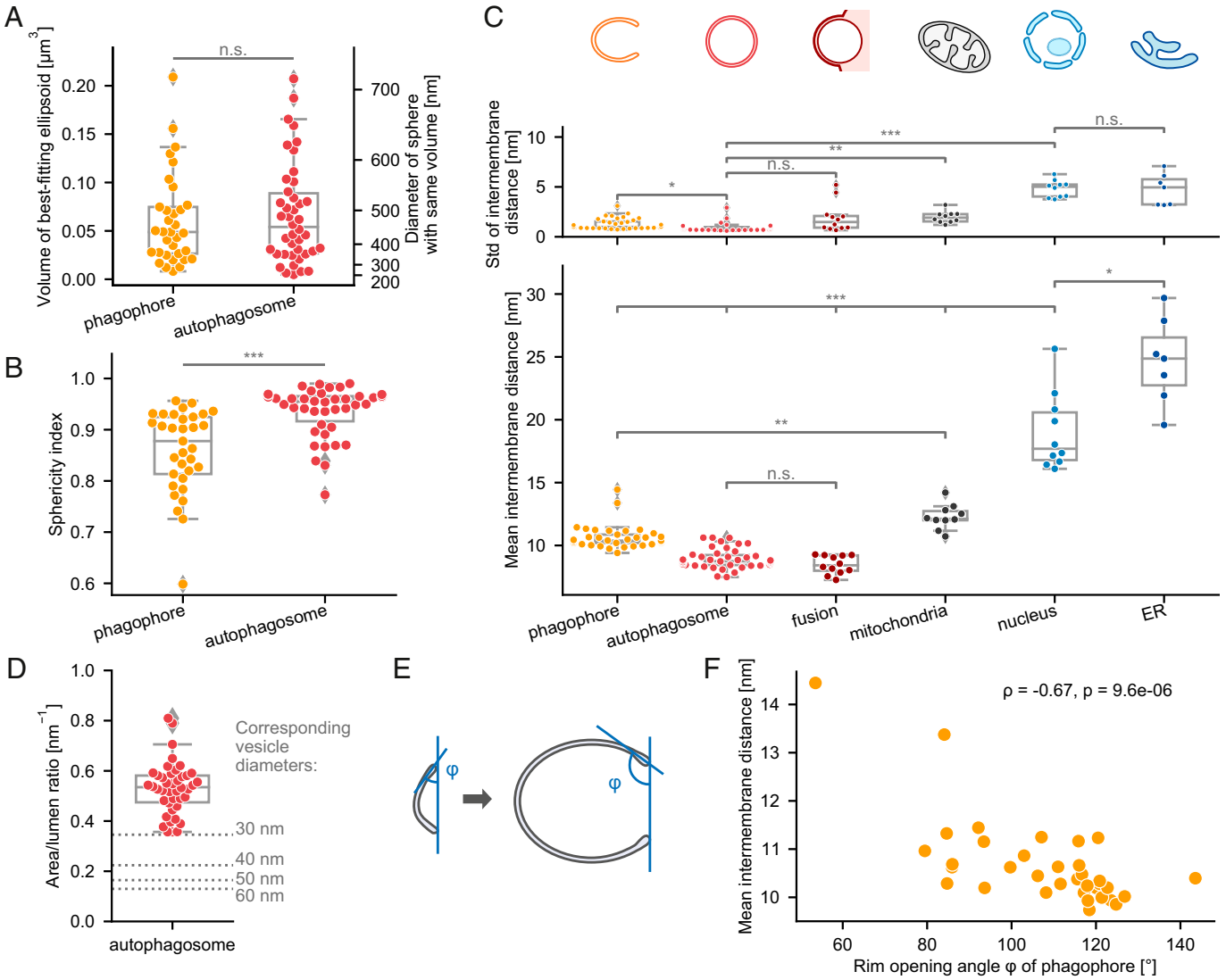

Fig. 5. Unique structural features of autophagic membranes. (*A*) Overall size of phagophores and autophagosomes estimated by the volumes of the best-fitting ellipsoids. The right axis indicates diameters of spheres with the same volume. (*B*) Sphericity index of phagophores and autophagosomes calculated from the best-fitting ellipsoids as $\sqrt[3]{(c^2/(ab))}$ with the ellipsoid axes a > b > c. (*C*) Intermembrane distance SDs (*Upper*) and mean (*Lower*) of various double-membrane organelles in the tomograms. Distances were calculated membrane middle to membrane middle; each point represents one structure. (*D*) Membrane area to intermembrane lumen ratio of closed autophagosomes. Gray dotted lines show the area/volume ratio of single-membrane vesicles with indicated diameters. (*E*) Scheme showing the rim opening angle φ for two phagophores in different stages of growth. (*F*) Intermembrane distance plotted against φ. The mean intermembrane distance correlates with the rim opening angle with a Spearman's correlation coefficient of −0.67, $P = 9.6{\cdot}10^{-6}$. Statistical analysis (*A* and *B*): Mann–Whitney *U* test; (*C*): Kruskal–Wallis H test and pairwise Games–Howell post hoc test. Autophagosomes $n = 42$, phagophores $n = 37$, fusion $n = 12$, mitochondria $n = 10$, nucleus $n = 10$, and ER $n = 7$. ***$P < 0.001$, **$P < 0.01$, *$P < 0.05$, n.s., $P \geq 0.05$.

feature to distinguish autophagosomes from other structures in the cell.

Because autophagosomes are close to perfect double-membrane spheres, their full structures can be extrapolated based on the tomogram data. This allows us to estimate for each observed autophagosome its total membrane area to intermembrane lumen ratio, yielding an average area/lumen ratio of 0.53 ± 0.10 nm^{-1} for closed autophagosomes (Fig. 5*D*). Of the two major processes thought to sustain phagophore growth, (I) vesicle fusion (44) and (II) direct lipid transfer (45), only the first adds volume to the intermembrane lumen. The reported size range of vesicles contributing to phagophore growth (4,12) is 30–60 nm for Atg9 and >60 nm for COPII (46), corresponding to a membrane area/volume ratio of 0.35–0.13 nm^{-1} (gray dotted lines, Fig. 5*D*). To define the in situ vesicle landscape, we measured the average diameter of vesicles observed within 100 nm of phagophores. On average, those vesicles have a diameter of 40 nm (*SI Appendix*, Fig. S5 *D* and *E*), which fits the expected range for Atg9 vesicles. By comparing the area/volume ratios of vesicles and autophagosomes (Fig. 5*D*), it is clear that if the intermembrane lumen of autophagosomes is built from vesicles alone, they do not contribute enough membrane to build the whole autophagosome, arguing for lipid transfer from the ER as a major membrane source during phagophore expansion. Assuming that the intermembrane lumen of autophagosomes does not change by other means, our data suggest that between 60–80% of the membrane area is derived from lipid transfer or synthesis (*SI Appendix*, Fig. S5*F*).

Interestingly, compared with closed autophagosomes, open phagophores show a significantly higher mean intermembrane spacing (10.6 ± 0.93 nm, $n = 37$, Mann–Whitney *U* test $P = 2.2{\cdot}10^{-11}$). This suggests that, counter to previous assumptions (17, 47), the intermembrane distance of phagophores is not constant but rather decreases during expansion.

Testing this hypothesis required a method for sorting the phagophores by degree of maturation. Having evaluated different parameters (*SI Appendix*, Note 1), we found the rim opening angle φ, calculated as the mean angle between a plane through the rim opening and tangent planes to the inner phagophore membrane at the rim, to be the most indicative (Fig. 5*E*). Throughout phagophore growth, φ should increase from around 0° in the initial membrane disk to 180° just before closure into a double-membrane sphere. As hypothesized, the mean intermembrane distance of the captured phagophores decreases significantly with φ (Fig. 5*F* and *SI Appendix*, Fig. S5 *G–I*). Taken together, the analysis yields conclusive evidence that the intermembrane distance decreases during autophagosome formation.

The Phagophore Rim Shape Transforms during Phagophore Growth. A striking feature of phagophores over autophagosomes is the highly curved rim at the opening of the cup-shaped structure. Notably, upon inspection of the tomograms, the rims of many phagophores appeared dilated (Fig. 6*A*). This is in contrast to the half toroid shape assumed in the literature (17, 47, 48), suggesting a direct impact on the rim curvature and bending energy.

To further investigate this phenomenon, we produced refined segmentations of 26 well-resolved phagophore rims and used custom scripts to detect their tips (*SI Appendix*, Fig. S6 *A–D*). The distances between the inner and outer membrane were measured orthogonally to the rim direction and mapped against their distance from the phagophore tip (*SI Appendix*, Fig. S6*D*). Plotting for each rim the mean intermembrane spacing against the distance from the tip (Fig. 6*B*) suggests that all analyzed rims show swelling. To determine whether indeed each rim is dilated, we next checked for the presence of maximum and minimum peaks in the intermembrane distance along each segmented rim, as well as their height and distance from the tip (*SI Appendix*, Fig. S6*E* and Table S3). The peak analysis confirms that all rims show a clear intermembrane distance maximum when moving from the tip toward the back, and maxima are present along the complete rim segment in most examples (*SI Appendix*, Fig. S6*E*). In contrast, minimum peaks, i.e., a constriction of the membranes after the swelling, are observed less consistently and therefore not analyzed in more detail. The position of the dilation maximum differs substantially between rims (17 ± 7 nm from the tip) (Fig. 6 *B* and *C*) and within the individual structures (median SD 2.6 nm). The intermembrane distances are less variable, with a mean maximum distance of 14.7 ± 1.8 nm and an average 10.9 ± 0.52 nm "base" distance for the back part of the rims, excluding the dilated region. By dividing the respective maximum and base distances, a "dilation factor" is obtained for each rim, with a mean value of 1.35 ± 0.15 (±SD) (Fig. 6*C*).

We speculated that the observed rim swelling might reduce the local mean curvature and thus the bending energy compared with a nondilated structure. By widening, the rim locally approaches the zero-energy catenoid shape with principal curvatures of equal magnitude but opposite sign. To test this hypothesis, we constructed artificial, nondilated versions of the analyzed rims, keeping the same membrane area, overall shape, and base intermembrane distance (*SI Appendix*, Fig. S6*F*). Fig. 5*D* shows the difference between the respective Helfrich bending energies (49) for the experimental and reference rims, normalized by the length of the rim segments and plotted against the dilation factor. While no clear trend is observed at dilation factors below 1.3, all experimental rims with a dilation factor >1.3 show a lower ($n = 7$ rims) or equal ($n = 1$ rim) bending energy compared with their nondilated counterparts. This suggests that strong swelling indeed decreases the bending energy at the rim, which helps stabilize the open phagophore state.

How does the shape of the rim evolve with phagophore growth? The maximum intermembrane spacing decreases strongly with the rim opening angle φ (Fig. 6*E* and *SI Appendix*, Fig. S6*G*). As a result, both the curvature at the rim tip and the bending energy per nanometer of rim increase during phagophore growth (Fig. 6*F* and *SI Appendix*, Fig. S6*H* and Table S4). Interestingly, these dynamic changes appear to have two independent and additive causes: first, a decrease in rim dilation (Fig. 6*E*) consistent with approaching locally a catenoid shape upon tightening of the neck, which decreases the energetic cost of a high first principal curvature. Second, however, the base distance also decreases with phagophore growth (Fig. 6*E*), which is most likely not a consequence but rather a driver of rim constriction. In this model, the decrease of phagophore membrane spacing increases the first principal curvature at the rim and therefore favors rim constriction to reduce the rim length and minimize the overall bending energy, thus promoting phagophore closure.

Discussion

Our structural analysis of autophagy in situ shows that phagophores are unique organelles that engulf mostly bulk cargo under starvation and form distinct contacts to the vacuole, ER, and rarely to LDs. Unexpectedly, their already thin intermembrane spacing decreases even more during growth, concomitant with a gradual decrease of rim swelling and increase of the rim curvature (Fig. 6*G*).

From the structures of closed autophagosomes, we estimate that only 20–40% of their membrane is contributed by fusion of vesicles. Note that 35–135 vesicles (60–40 nm diameter) would suffice to build the intermembrane lumen of a typical autophagosome and that no processes have been described to date that actively reduce the intermembrane lumen of phagophores. Lipid transfer should then contribute 60–80% of the autophagosome membrane, supported by the frequently observed close contacts of the phagophore rim with the ER and NM. Even if the luminal volume expands slightly to counteract the high rim curvature and tight membrane spacing, this will only decrease the number of needed vesicles and necessitate even more lipid transfer (*SI Appendix*, Fig. S5*J*).

In yeast, Atg9 vesicles contribute mainly to the initial nucleation stage (11), whereas other membrane sources, such as COPII vesicles, are thought to contribute to both early and late phagophore growth (14). The decreasing intermembrane distance from early to late phagophores implies that their area/lumen ratio is smaller initially and increases as they grow. This is in line with a model in which vesicles mainly contribute to the initial stages, whereas lipid transfer becomes the major membrane source later during phagophore growth (Fig. 6G). How does the proposed shift in membrane sources affect phagophore growth? In the absence of other mechanisms controlling the luminal volume, the relative rates of vesicle fusion and lipid transfer determine the rate of phagophore thinning. Phagophore thinning increases, in turn, the curvature at the rim, which should accelerate constriction toward an almost closed phagophore. Thus, we speculate that the size of the final autophagosome might be limited by the fusion rate and total number of contributing vesicles. In line with this, the captured autophagosomes show no correlation between intermembrane distance and size (*SI Appendix*, Fig. S5*J*). Note that this model assumes a sufficient abundance of curvature generators stabilizing the rim (17) and a continued

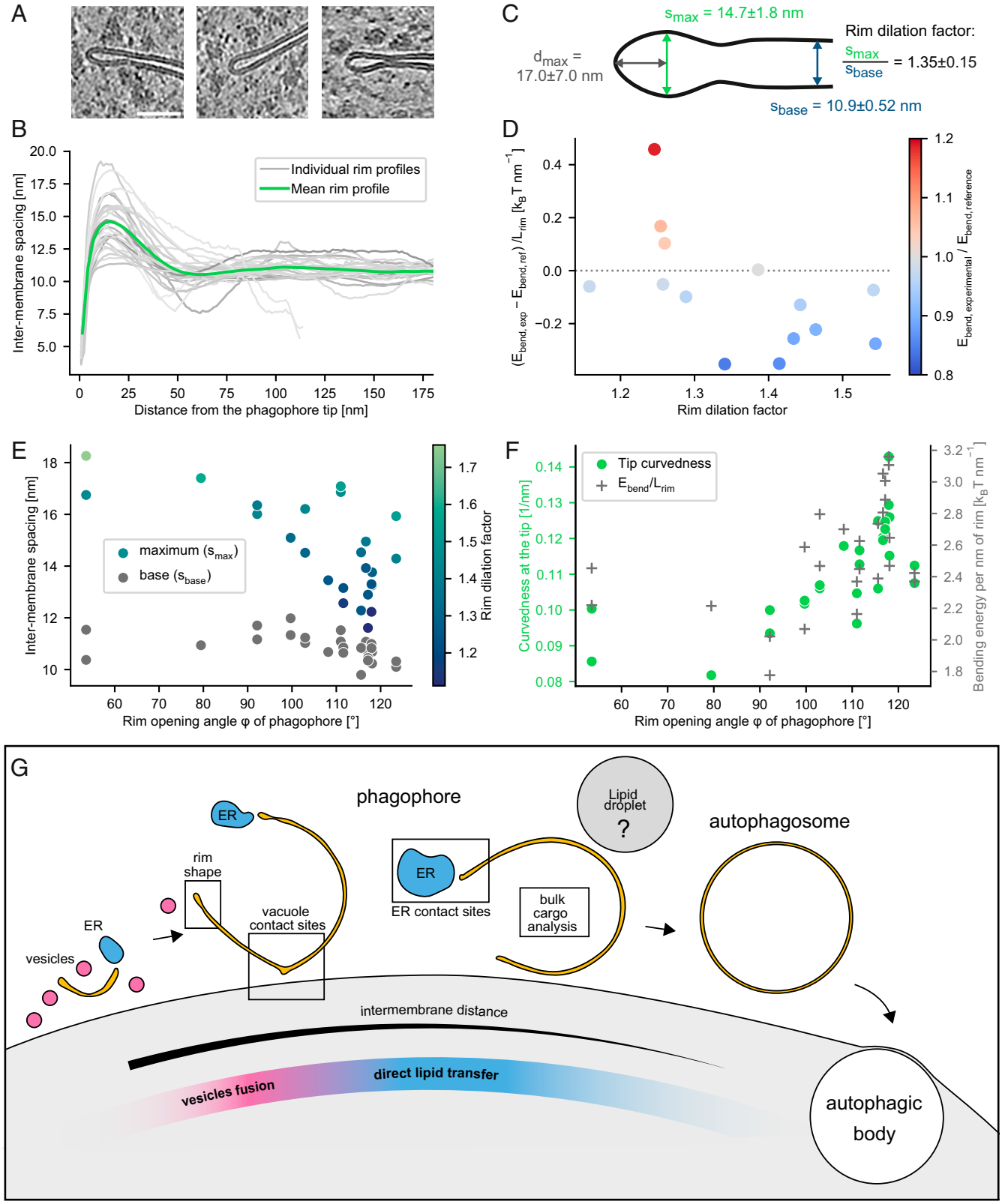

Fig. 6. Characterization of the phagophore rim and model of autophagosome biogenesis. (*A*) Example tomogram snapshots of phagophore rims, scale bar: 50 nm. (*B*) Mean (green) and individual rim profiles (gray) for all analyzed rims (n = 26), plotted as intermembrane distance versus distance from the tip. (*C*) Rim shape parameters, including intermembrane spacing in the back (s_{back}) and at the swelling maximum (s_{max}) and the distance of the maximum to the tip (d_{max}). Mean and SD calculated from 26 rims. (*D*) Effect of rim swelling on the bending energy of experimental ($E_{bend,\ exp}$) versus hypothetical nonswollen reference rims ($E_{bend,\ ref}$) (n = 14). The experimental is smaller than the reference bending energy for most cases with a dilation factor (s_{max}/s_{back}) of 1.3 or higher. (*E*) Rim intermembrane spacing (maximum and back) versus rim opening angle φ. Spearman's rank correlation: $\rho = -0.64$, $P = 4.1 \cdot 10^{-4}$ (max. spacing); $\rho = -0.63$, $P = 5.4 \cdot 10^{-4}$ (back spacing); and $\rho = -0.44$, $P = 0.025$ (dilation factor) (n = 26). (*F*) Membrane curvedness within 1.408 nm (one binned pixel) of the tip (green, left y axis) and bending energy per nanometer of rim (gray, right y axis) plotted against φ. Spearman's rank correlation: $\rho = 0.77$, $P = 4.1 \cdot 10^{-6}$ (curvedness) and $\rho = 0.53$, $P = 0.0057$ (bending energy) (n = 26). (*G*) Summary of ultrastructural features of autophagy and autophagosome biogenesis model: vesicles (magenta) are major contributors during early biogenesis, while direct lipid transfer from the ER (blue) is the main source for membrane growth in later stages. This results in a decrease of the intermembrane spacing and increase of rim curvature, favoring rim constriction toward the closed autophagosome.

flow of lipids into the phagophore during growth. Possible drivers for this directional transport are local lipid synthesis in the ER (45), a high local concentration of Atg8 in the phagophore favoring lipid influx in an osmosis-like process (50), or differences in membrane curvature (Fig. 4*E*). How the recruitment of the ESCRT machinery for phagophore closure (51) relates to the maturation of the rim and to the final autophagosome size remains to be determined.

Our analysis of the organelle interactome of autophagic structures shows that phagophores form very polarized contact sites. The most prominent is the ER–rim contact site, which likely functions in Atg2-mediated lipid transfer (15). Based on fluorescence microscopy experiments, Atg2 localizes to the phagophore rim (3, 33). In agreement with this, we identified electron-dense structures spanning across the ER–rim contacts with lengths in the expected range for Atg2 (39) (*SI Appendix*, Fig. S4*C*). Calculations based on our analysis suggest that less than 100 copies of Atg2 per phagophore would suffice to build an average-sized autophagosome (*SI Appendix*, Note 2). This could explain why so few connecting densities are found at the contact sites.

Even more frequently than phagophore–ER contacts, we observe interactions with the vacuole, preferentially at the back or side of the phagophore. The heterogeneity of these contacts is consistent with a recent study showing that the anchoring of the PAS machinery to the vacuole is an avidity-driven process mediated by locally clustered Vac8 (52). If the tethering of the phagophore membrane is also mediated by Vac8, variable cluster sizes could explain the variety of contact shapes observed. As to why phagophores are tethered to the vacuole, we suggest that this arrangement allows the starving cell to produce many autophagosomes one after the other while keeping the autophagy machinery at a defined location for growth, maturation, and fusion. In fact, we often observe partially enveloped autophagic bodies in the vacuole directly next to open phagophores (Fig. 1*D* and *SI Appendix*, Fig. S2*D*), suggesting that the same site was used at least twice in quick succession.

Finally, the present study can serve as blueprint for studying organelle biogenesis processes. For example, it would be interesting to investigate whether characteristics such as the thin intermembrane spacing and its decrease during growth are conserved from yeast to mammalian autophagy, and to characterize the mammalian subcellular environment of autophagosome biogenesis, which was previously described as an "ER cradle" (6). In addition, fluorescent targeting of proteins with temporally distinct roles could help to relate ultrastructural stages to the action of different molecular players. Regardless of the target process, induction of organelle formation, fluorescent tagging of the growing structure, and genetic or pharmacological manipulation to accumulate intermediates are essential steps to capture the intermediates by correlative cryo-ET. Although it is static by nature, in situ tomography is not limited to resolving protein structures but can also provide information on the dynamic morphology of membranes and direct measurements for the biophysical characterization and modeling of transient cellular processes.

Methods

Yeast Strains. A list of budding yeast (*S. cerevisiae*) strains used in this study is provided in *SI Appendix*, Table S5. All of the yeast strains were based on the DF5 background. Standard protocols for transformation, mating, sporulation, and tetrad dissection were used for yeast manipulations (53). Chromosomally tagged strains and knockout strains were constructed using a PCR-based integration strategy (54). Standard cloning techniques were used.

Live-Cell Fluorescence Microscopy. A detailed protocol of the live-cell fluorescence imaging is available under https://www.protocols.io/view/yeast-cells-live-fluorescence-imaging-n92ldzqjnv5b/v1. For fluorescence microscopy, yeast cells were grown in synthetic growth medium supplemented with all essential amino acids and 2% glucose. The next day, cells were diluted to optical density (OD600) 0.1 and grown until midlog phase (0.5–0.8 OD600) before imaging. Microscopy slides were pretreated with 1 mg mL^{-1} concanavalin A solution. Widefield imaging was performed at the Imaging Facility of the Max Planck Institute of Biophysics using a Nikon Ti2 Eclipse microscope comprising an Olympus Apo total internal reflection fluorescence 100× 1.49 oil objective and a Hamamatsu ORCA-Flash 4.0 LT+ Digital complementary metal oxide semiconductor camera. The images were deconvolved using the Nikon NIS Elements Batch Deconvolution Tool (automatic function). Image analysis was performed using the CellCounter plugin (https://imagej.nih.gov/ij/plugins/cell-counter.html) in ImageJ 1.53 (https://imagej.nih.gov/ij/, RRID: SCR_003070).

Cryo-ET Sample Preparation. A detailed protocol of the correlative cryo-ET workflow is available under https://www.protocols.io/view/3d-correlative-fib-milling-and-cryo-et-of-autophag-e6nvwkz4wvmk/v1.

Starvation and plunge freezing. Yeast cultures were inoculated from overnight cultures in YPD medium (1% yeast extract, 2% peptone, and 2% glucose) to an OD600 of 0.15 and grown at 30 °C to an OD600 of 0.8. At this point, medium was switched to SD-N (synthetic minimal medium lacking nitrogen; 0.17% yeast nitrogen base without amino acids and ammonium sulfate, supplemented with 2% glucose) and cells were incubated for a time span of 0.5–3 h at 30 °C. For 3D correlation on the grid, 1 μm Dynabeads (Dynabeads MyOne carboxylic acid No. 65011, Thermo Fisher Scientific) were added to the cells at a dilution of 1:20. Grids (200 Mesh Cu SiO_2 R1/4, Quantifoil) were plasma cleaned for 30 s before plunging. Four microliters of starved cell solution with beads was applied on the grid, blotted, and plunged in ethane–propane with a Vitrobot Mark IV (settings: blot force = 8, blot time = 10 s, room temperature).

Cryo-fluorescence microscopy and correlative FIB milling. Grids were mounted on modified autogrids with cut-out for FIB milling, and fluorescence image stacks were acquired on a cryo-confocal microscope (Leica SP8 with Cryo-Stage) equipped with a 50×/0.9 numerical aperture objective (Leica Objective No. 506520) and two HyD detectors. Stacks (step size 300 nm, x–y pixel size 85 nm) were acquired using 488-nm and 552-nm laser excitation for eGFP- and mCherry-labeled proteins, respectively. In the case of eGFP-only strains (eGFP-Atg8 and eGFP-Ede1/*ypt7Δ*), signal from autofluorescent Dynabeads was acquired as second channel corresponding to red emission wavelengths to easily distinguish fiducial beads from cellular signal. Stacks were deconvolved using Huygens Essential (20.10.0, Scientific Volume Imaging, https://svi.nl/Huygens-Software, RRID: SCR_014237). Target sites corresponding to Atg8 puncta or Ede1 END cargo were 3D correlated to SEM/IB images in the FIB/SEM microscope (FIB Scios and Aquilos, Thermo Fisher Scientific) using the 3D-Correlation Toolbox (3DCT) (https://3dct.semper.space/) (23). Lamellae were milled in correlated sites as described in a previously published protocol (24). In a few cases (e.g., *SI Appendix*, Fig. 1*A*), a widefield microscope integrated in the FIB/SEM chamber (METEOR, delmic) was used to confirm the presence of fluorescence signal in the lamella, as previously published (55).

Cryo-EM Data Acquisition. Tomograms were acquired on a TEM (Titan Krios, field emission gun 300 kV, Thermo Fisher Scientific) equipped with an energy filter (Quantum K2, Gatan) and a direct detection camera (K2 Summit, Gatan) at a magnification of 42,000× (pixel size 3.52 Å) and defocus ranging from −5 to −3.5 μm. Positions for tomogram acquisition were determined by correlation of fluorescence data to TEM images of the grid squares containing lamellae (3DCT), followed by inspection of low-magnification lamella images. Frames were recorded in dose-fractionation mode, with a total dose of 120 e^-/A^2 per tilt series using SerialEM 3.9.0 (RRID: SCR_017293, https://bio3d.colorado.edu/SerialEM/) (56). A dose-symmetric tilt scheme was used with an increment of 2° in a total range of ±60° from a starting angle of 10° (+ or −) to compensate for lamella pretilt (mostly around 11°). Frames were aligned using MotionCorr2 (v.1.4.0, https://emcore.ucsf.edu/ucsf-software) (57), and reconstruction was performed in IMOD (v.4.10.49, RRID:SCR_003297, https://bio3d.colorado.edu/imod/) by using the TomoMAN wrapper scripts (58).

Tomogram Analysis. Here, we give a brief overview of the analysis workflows used in this study. Detailed descriptions of all analyses are provided in the *SI Appendix, SI Methods*.

Segmentation and visualization. Tomograms at 2× binning (IMOD bin 4) with a nominal pixel size of 1.408 nm were denoised using cryo-CARE on tomograms reconstructed from odd/even frames (59). Membrane middles (middle of phospholipid bilayer) were detected automatically using TomoSegMemTV (04/2014, https://sites.google.com/site/3demimageprocessing/tomosegmemtv) (40) and selected in Amira 2019 (Thermo Fisher Scientific, https://www.thermofisher.com/de/de/home/electron-microscopy/products/software-em-3d-vis/amira-software.html). Segmentations for display purposes (Fig. 1 *I–L*) were manually refined in Amira, Gaussian filtered, and displayed in ChimeraX 1.2.5 (https://www.cgl.ucsf.edu/chimerax/, RRID: SCR_015872) (60). For analyses of membrane curvature (phagophore rims and contact sites), the automatic segmentations were refined manually in Amira. Mesh generation from the filled segmentation and curvature determination was done using PyCurv (09/2020, https://github.com/kalemaria/pycurv) (61) using a radius hit of 8 nm. Visualizations of different parameters on segmented membranes (Fig. 4 and *SI Appendix*, Fig. 3 *D* and *E* and 4 *A*) were produced with PyVista 0.27.4 (https://docs.pyvista.org/) (62).

Cargo analysis. For each captured autophagic structure, the general type of cargo (ribosomes, ribosomes + other cargo, and selective) was annotated from visual inspection of the tomograms. Ribosome positions were determined by template matching with StopGAP 0.7.0 (63), followed by subtomogram averaging and classification using Warp/M (64) and Relion 3.1.2 (65). The positions in the refined particle list were combined with tomogram segmentations to calculate ribosome densities and nearest neighbor distances in- and outside of the autophagic structures (*SI Appendix, SI Methods*).

Contact sites. For all contact site analyses, tomograms from the *ypt7Δ* strain were excluded since the overall cellular architecture in this strain was disturbed by accumulation of medium-sized vacuoles (66) (*SI Appendix*, Fig. 1*I*). Nearest distances, interaction areas, and deformations were measured and determined in IMOD as described in the *SI Appendix, SI Methods*. To analyze phagophore–vacuole and phagophore–ER contact sites in detail, we used PyCurv to determine local membrane curvatures and analyzed the resulting meshes with custom python scripts (*SI Appendix, SI Methods*).

Membrane morphology of autophagic structures. Intermembrane distances were determined from the automatically generated membrane segmentations using the refined minimum distance algorithm (*SI Appendix, SI Methods*). For size and sphericity measurements, ellipsoid fits into the segmented membranes were performed with an iterative algorithm adapted from Kovac et al. (67). The ellipsoid fits and mean intermembrane distances were further used to estimate the area-to-lumen ratios of autophagosomes. To assess the completeness of phagophores, we calculated for each structure its "rim opening angle φ", defined as the angle between a plane through the phagophore rim and tangential planes to the phagophore membrane close to the rim. Meshes generated from refined segmentations of phagophore rim segments were analyzed with custom python scripts to quantify rim swelling, report site-specific curvatures, and estimate bending energies. A detailed description of all algorithms and discussion on different completeness parameters is given in the *SI Appendix, SI Methods*.

Statistics. Statistical analyses were performed with the statistical analysis package in scipy 1.6.2 (scipy.stats) and the pingouin package (v.0.3.11, https://pingouin-stats.org/) (68), using the tests indicated in each respective analysis. In general, statistical analysis of differences between two groups was performed using the Mann–Whitney *U* test for independent and the Wilcoxon signed-rank test for dependent samples. Comparison of more groups was performed with the Kruskal–Wallis H test and pairwise Games–Howell post hoc test. Correlation between variables was assessed with Spearman's rank correlation coefficient.

Data, Materials, and Software Availability. All tilt series of autophagic structures analyzed in this study are available at EMPIAR-11166 (69). Representative tomograms are additionally available in the Electron Microscopy Data Bank under the following accession codes: EMD-15526 (70) (Fig. 1*E*), EMD-15545 (71) (Fig. 1*F*), EMD-15546 (72) (Fig. 1*G*), EMD-15547 (73) (Fig. 1*H*), EMD-15549 (74) (Fig. 4*A*), and EMD-15548 (75) (Fig. 4 *D* and *F*). Source data for all plots are deposited under https://zenodo.org/record/6607443 (76).

Custom python code written for this study is available on GitHub (https://github.com/Anna-Bieber/autophagy-tomo-analysis) (77), and published on Zenodo (78).

ACKNOWLEDGMENTS. We thank J. Plitzko for microscope support; L. Bas, B. Engel, W. Wietrzynski, S. Klumpe, S. Khavnekar, R. Bhaskara, and S. von Bülow for discussions; and D. Hollenstein and C. Kraft for critical reading of the manuscript. This study was supported by the Max Planck Gesellschaft and funded in part by Aligning Science Across Parkinson's ASAP-000282 (B.A.S. and W.B.) and ASAP-000350 (G.H.) through the Michael J. Fox Foundation for Parkinson's Research. A.B. was supported by a PhD fellowship of the Boehringer Ingelheim Fonds.

Author affiliations: [a]Department of Molecular Structural Biology, Max Planck Institute of Biochemistry, 82152 Martinsried, Germany; [b]Department of Molecular Machines and Signaling, Max Planck Institute of Biochemistry, 82152 Martinsried, Germany; [c]Aligning Science Across Parkinson's (ASAP) Collaborative Research Network, Chevy Chase, MD 20815; [d]Human Technopole, 20157 Milan, Italy; [e]Mechanisms of Cellular Quality Control, Max Planck Institute of Biophysics, 60438 Frankfurt a. M., Germany; [f]CryoEM Technology, Max Planck Institute of Biochemistry, 82152 Martinsried, Germany; [g]Department of Molecular Metabolism, Harvard T. H. Chan School of Public Health, Boston, MA 02115; [h]Department of Theoretical Biophysics, Max Planck Institute of Biophysics, 60438 Frankfurt a. M., Germany; and [i]Institute of Biophysics, Goethe University Frankfurt, 60438 Frankfurt a. M., Germany

Author contributions: A.B., C.C., P.S.E., F.B., B.A.S., W.B., and F.W. designed research; A.B., C.C., P.S.E., F.B., F.F., C.-W.L., D.L., G.H., and F.W. performed research; A.B., C.C., F.F., C.-W.L., and F.W. contributed new reagents/analytic tools; A.B., C.C., P.S.E., F.F., F.B., C.-W.L., D.L., G.H., and F.W. analyzed data; and A.B., C.C., P.S.E., F.F., C.-W.L., D.L., G.H., B.A.S., W.B., and F.W. wrote the paper.

Reviewers: A.C., Technion Israel Institute of Technology The Ruth and Bruce Rappaport Faculty of Medicine; and A.V., California Institute of Technology.

Competing interest statement: B.A.S. holds additional appointments as an Honorary Professor at Technical University of Munich, Germany and adjunct faculty at St. Jude Children's Research Hospital, Memphis, TN, USA and is on the Scientific Advisory Boards of Interline Therapeutics and BioTheryX. B.A.S. is co-inventor of intellectual property related to DCN1 inhibitors (unrelated to this work) licensed to Cinsano. W.B. holds additional appointments as honorary Professor at the Technical University Munich and Distinguished Professor at ShanghaiTech University and is a member of the Life Science Advisory Board of Thermo Fisher Scientific.

1. Y. Ohsumi, Historical landmarks of autophagy research. *Cell Res.* **24**, 9–23 (2013).
2. K. Suzuki, Y. Ohsumi, Molecular machinery of autophagosome formation in yeast, *Saccharomyces cerevisiae*. *FEBS Lett.* **581**, 2156–2161 (2007).
3. K. Suzuki, M. Akioka, C. Kondo-Kakuta, H. Yamamoto, Y. Ohsumi, Fine mapping of autophagy-related proteins during autophagosome formation in *Saccharomyces cerevisiae*. *J. Cell Sci.* **126**, 2534–2544 (2013).
4. E.-L. Eskelinen, F. Reggiori, M. Baba, A. L. Kovács, P. O. Seglen, Seeing is believing: The impact of electron microscopy on autophagy research. *Autophagy* **7**, 935–956 (2011).
5. M. Baba, K. Takeshige, N. Baba, Y. Ohsumi, Ultrastructural analysis of the autophagic process in yeast: Detection of autophagosomes and their characterization. *J. Cell Biol.* **124**, 903–913 (1994).
6. M. Hayashi-Nishino *et al.*, A subdomain of the endoplasmic reticulum forms a cradle for autophagosome formation. *Nat. Cell Biol.* **11**, 1433–1437 (2009).
7. P. Ylä-Anttila, H. Vihinen, E. Jokitalo, E. L. Eskelinen, 3D tomography reveals connections between the phagophore and endoplasmic reticulum. *Autophagy* **5**, 1180–1185 (2009).
8. H. Nakatogawa, Mechanisms governing autophagosome biogenesis. *Nat. Rev. Mol. Cell Biol.* **21**, 439–458 (2020).
9. T. Nishimura, S. A. Tooze, Emerging roles of ATG proteins and membrane lipids in autophagosome formation. *Cell Discov.* **6**, 32 (2020).
10. D. M. Hollenstein *et al.*, Vac8 spatially confines autophagosome formation at the vacuole in *S. cerevisiae*. *J. Cell Sci.* **132**, jcs235002 (2019).
11. H. Yamamoto *et al.*, Atg9 vesicles are an important membrane source during early steps of autophagosome formation. *J. Cell Biol.* **198**, 219–233 (2012).
12. J. Sawa-Makarska *et al.*, Reconstitution of autophagosome nucleation defines Atg9 vesicles as seeds for membrane formation. *Science (80-.)* **369**, eaaz7714 (2020).
13. A. H. Bahrami, M. G. Lin, X. Ren, J. H. Hurley, G. Hummer, Scaffolding the cup-shaped double membrane in autophagy. *PLOS Comput. Biol.* **13**, e1005817 (2017).
14. T. Shima, H. Kirisako, H. Nakatogawa, COPII vesicles contribute to autophagosomal membranes. *J. Cell Biol.* **218**, 1503–1510 (2019).
15. T. Osawa *et al.*, Atg2 mediates direct lipid transfer between membranes for autophagosome formation. *Nat. Struct. Mol. Biol.* **26**, 281–288 (2019).
16. Z. Xie, U. Nair, D. J. Klionsky, Atg8 controls phagophore expansion during autophagosome formation. *Mol. Biol. Cell* **19**, 3290–3298 (2008).
17. Y. Sakai, I. Koyama-Honda, M. Tachikawa, R. L. Knorr, N. Mizushima, Modeling membrane morphological change during autophagosome formation. *iScience* **23**, 101466 (2020).
18. J. Collado *et al.*, Tricalbin-mediated contact sites control ER curvature to maintain plasma membrane integrity. *Dev. Cell* **51**, 476–487.e7 (2019).
19. C. E. Zimmerli *et al.*, Nuclear pores dilate and constrict in cellulo. *Science (80-.)* **374**, abd9776 (2021).
20. Y. Kamada *et al.*, Tor directly controls the Atg1 kinase complex to regulate autophagy. *Mol. Cell. Biol.* **30**, 1049–1058 (2010).

21. X. Wen, D. J. Klionsky, An overview of macroautophagy in yeast. *J. Mol. Biol.* **428** (9 Pt A), 1681–1699 (2016).
22. F. Wilfling *et al.*, A selective autophagy pathway for phase-separated endocytic protein deposits. *Mol. Cell* **80**, 764–778.e7 (2020).
23. J. Arnold *et al.*, Site-specific cryo-focused ion beam sample preparation guided by 3D correlative microscopy. *Biophys. J.* **110**, 860–869 (2016).
24. A. Bieber, C. Capitanio, F. Wilfling, J. Plitzko, P. S. Erdmann, Sample preparation by 3D-correlative focused ion beam milling for high-resolution cryo-electron tomography. *J. Vis. Exp.* **176**, e62886 (2021).
25. T. Kirisako *et al.*, Formation process of autophagosome is traced with Apg8/Aut7p in yeast. *J. Cell Biol.* **147**, 435–446 (1999).
26. G. Zaffagnini, S. Martens, Mechanisms of selective autophagy. *J. Mol. Biol.* **428** (9 Pt A), 1714–1724 (2016).
27. M. Baba, M. Osumi, S. V. Scott, D. J. Klionsky, Y. Ohsumi, Two distinct pathways for targeting proteins from the cytoplasm to the vacuole/lysosome. *J. Cell Biol.* **139**, 1687–1695 (1997).
28. A. Khaminets *et al.*, Regulation of endoplasmic reticulum turnover by selective autophagy. *Nature* **522**, 354–358 (2015).
29. K. Mochida *et al.*, Receptor-mediated selective autophagy degrades the endoplasmic reticulum and the nucleus. *Nature* **522**, 359–362 (2015).
30. M. Umekawa, D. J. Klionsky, The cytoplasm-to-vacuole targeting pathway: A historical perspective. *Int. J. Cell Biol.* **2012**, 142634 (2012).
31. C. Bertipaglia *et al.*, Higher-order assemblies of oligomeric cargo receptor complexes form the membrane scaffold of the Cvt vesicle. *EMBO Rep.* **17**, 1044–1060 (2016).
32. K. Suzuki *et al.*, The pre-autophagosomal structure organized by concerted functions of APG genes is essential for autophagosome formation. *EMBO J.* **20**, 5971–5981 (2001).
33. M. Graef, J. R. Friedman, C. Graham, M. Babu, J. Nunnari, ER exit sites are physical and functional core autophagosome biogenesis components. *Mol. Biol. Cell* **24**, 2918–2931 (2013).
34. T. Shpilka *et al.*, Lipid droplets and their component triglycerides and steryl esters regulate autophagosome biogenesis. *EMBO J.* **34**, 2117–2131 (2015).
35. J. Schepers, C. Behl, Lipid droplets and autophagy-links and regulations from yeast to humans. *J. Cell. Biochem.* **122**, 602–611 (2021).
36. A. P. Velázquez, T. Tatsuta, R. Ghillebert, I. Drescher, M. Graef, Lipid droplet-mediated ER homeostasis regulates autophagy and cell survival during starvation. *J. Cell Biol.* **212**, 621–631 (2016).
37. T. Kotani, H. Kirisako, M. Koizumi, Y. Ohsumi, H. Nakatogawa, The Atg2-Atg18 complex tethers pre-autophagosomal membranes to the endoplasmic reticulum for autophagosome formation. *Proc. Natl. Acad. Sci. U.S.A.* **115**, 10363–10368 (2018).
38. S. Chowdhury *et al.*, Insights into autophagosome biogenesis from structural and biochemical analyses of the ATG2A-WIPI4 complex. *Proc. Natl. Acad. Sci. U.S.A.* **115**, E9792–E9801 (2018).
39. T. Osawa, N. N. Noda, Atg2: A novel phospholipid transfer protein that mediates de novo autophagosome biogenesis. *Protein Sci.* **28**, 1005–1012 (2019).
40. A. Martinez-Sanchez, I. Garcia, S. Asano, V. Lucic, J.-J. Fernandez, Robust membrane detection based on tensor voting for electron tomography. *J. Struct. Biol.* **186**, 49–61 (2014).
41. E. D. Sneed, R. L. Folk, Pebbles in the Lower Colorado River, Texas a Study in Particle Morphogenesis. *The Journal of Geology* **66**, 114–150 (1958).
42. K. Tsuboyama *et al.*, The ATG conjugation systems are important for degradation of the inner autophagosomal membrane. *Science (80-.)* **354**, 1036–1041 (2016).
43. N. Nguyen, V. Shteyn, T. J. Melia, Sensing membrane curvature in macroautophagy. *J. Mol. Biol.* **429**, 457–472 (2017).
44. T. J. Melia, A. H. Lystad, A. Simonsen, Autophagosome biogenesis: From membrane growth to closure. *J. Cell Biol.* **219**, e202002085 (2020).
45. M. Schütter, P. Giavalisco, S. Brodesser, M. Graef, Local Fatty Acid Channeling into Phospholipid Synthesis Drives Phagophore Expansion during Autophagy. *Cell* **180**, 135–149.e14 (2020).
46. K. Matsuoka *et al.*, COPII-coated vesicle formation reconstituted with purified coat proteins and chemically defined liposomes. *Cell* **93**, 263–275 (1998).
47. R. L. Knorr, R. Dimova, R. Lipowsky, Curvature of double-membrane organelles generated by changes in membrane size and composition. *PLoS One* **7**, e32753 (2012).
48. J. Agudo-Canalejo *et al.*, Wetting regulates autophagy of phase-separated compartments and the cytosol. *Nature* **591**, 142–146 (2021).
49. W. Helfrich, Elastic properties of lipid bilayers: Theory and possible experiments. *Z. Naturforsch. C* **28**, 693–703 (1973).
50. Y. Zhang, J. Ge, X. Bian, A. Kumar, Quantitative models of lipid transfer and membrane contact formation. *Contact* **5**, (2022).
51. F. Zhou *et al.*, Rab5-dependent autophagosome closure by ESCRT. *J. Cell Biol.* **218**, 1908–1927 (2019).
52. D. M. Hollenstein *et al.*, Spatial control of avidity regulates initiation and progression of selective autophagy. *Nat. Commun.* **12**, 7194 (2021).
53. M. J. Dunham, M. W. Gartenberg, G. W. Brown, *Methods in Yeast Genetics and Genomics*: a Cold Spring Harbor Laboratory Course Manual, Cold Spring Harbor Laboratory Press, 2015th Ed. (2015).
54. M. Knop *et al.*, Epitope tagging of yeast genes using a PCR-based strategy: More tags and improved practical routines. *Yeast* **15** (10B), 963–972 (1999).
55. M. Smeets *et al.*, Integrated cryo-correlative microscopy for targeted structural investigation in situ. *Micros. Today* **29**, 20–25 (2021).
56. D. N. Mastronarde, Automated electron microscope tomography using robust prediction of specimen movements. *J. Struct. Biol.* **152**, 36–51 (2005).
57. S. Q. Zheng *et al.*, MotionCor2: Anisotropic correction of beam-induced motion for improved cryo-electron microscopy. *Nat. Methods* **14**, 331–332 (2017).
58. W. Wan, williamnwan/TOMOMAN: TOMOMAN 08042020. *Zenodo* (2020). 10.5281/ZENODO.4110737.
59. T. O. Buchholz, M. Jordan, G. Pigino, F. Jug, *Cryo-CARE: Content-aware image restoration for cryo-transmission electron microscopy data.* Proceedings - International Symposium on Biomedical Imaging (IEEE Computer Society), pp. 502–506 (2019).
60. E. F. Pettersen *et al.*, UCSF ChimeraX: Structure visualization for researchers, educators, and developers. *Protein Sci.* **30**, 70–82 (2021).
61. M. Salfer, J. F. Collado, W. Baumeister, R. Fernández-Busnadiego, A. Martínez-Sánchez, Reliable estimation of membrane curvature for cryo-electron tomography. *PLOS Comput. Biol.* **16**, e1007962 (2020).
62. C. Sullivan, A. Kaszynski, PyVista: 3D plotting and mesh analysis through a streamlined interface for the Visualization Toolkit (VTK). *J. Open Source Softw.* **4**, 1450 (2019).
63. W. Wan, S. Khavnekar, J. Wagner, P. Erdmann, W. Baumeister, STOPGAP: A software package for subtomogram averaging and refinement. *Microsc. Microanal.* **26**, 2516–2516 (2020).
64. D. Tegunov, P. Cramer, Real-time cryo-electron microscopy data preprocessing with Warp. *Nat. Methods* **16**, 1146–1152 (2019).
65. J. Zivanov *et al.*, New tools for automated high-resolution cryo-EM structure determination in RELION-3. *eLife* **7**, 42166 (2018).
66. Y. Chen *et al.*, A Vps21 endocytic module regulates autophagy. *Mol. Biol. Cell* **25**, 3166–3177 (2014).
67. B. Kovac, J. Fehrenbach, L. Guillaume, P. Weiss, FitEllipsoid: A fast supervised ellipsoid segmentation plugin. *BMC Bioinformatics* **20**, 142 (2019).
68. R. Vallat, Pingouin: Statistics in Python. *J. Open Source Softw.* **3**, 1026 (2018).
69. C. Capitanio, A. Bieber, P. S. Erdmann, B. A. Schulman, W. Baumeister, F. Wilfling, In situ cryo-electron tomography of autophagic structures in S. cerevisiae. EMPIAR, https://www.ebi.ac.uk/empiar/EMPIAR-11166/. Accessed 8 September 2022.
70. A. Bieber, C. Capitanio, P. S. Erdmann, B. A. Schulman, W. Baumeister, F. Wilfling, In situ cryo-electron tomogram of a bulk autophagy phagophore in S. cerevisiae. EMDB, https://www.ebi.ac.uk/emdb/EMD-15526. Accessed 8 September 2022.
71. C. Capitanio, A. Bieber, P. S. Erdmann, B. A. Schulman, W. Baumeister, F. Wilfling, In situ cryo-electron tomogram of a bulk autophagy phagophore in S. cerevisiae #2. EMDB, https://www.ebi.ac.uk/emdb/EMD-15545. Accessed 8 September 2022.
72. A. Bieber, C. Capitanio, P. S. Erdmann, B. A. Schulman, W. Baumeister, F. Wilfling, In situ cryo-electron tomogram of a bulk autophagy autophagosome with END cargo in S. cerevisiae #1. EMDB, https://www.ebi.ac.uk/emdb/EMD-15546. Accessed 8 September 2022.
73. A. Bieber, C. Capitanio, P. S. Erdmann, B. A. Schulman, W. Baumeister, F. Wilfling, In situ cryo-electron tomogram of a bulk autophagy autophagosome fusing with the vacuole in S. cerevisiae #1. EMDB, https://www.ebi.ac.uk/emdb/EMD-15547. Accessed 8 September 2022.
74. A. Bieber, C. Capitanio, P. S. Erdmann, B. A. Schulman, W. Baumeister, F. Wilfling, In situ cryo-electron tomogram of a bulk autophagy phagophore in S. cerevisiae #4. EMDB, https://www.ebi.ac.uk/emdb/EMD-15549. Accessed 8 September 2022.
75. C. Capitanio, A. Bieber, P. S. Erdmann, B. A. Schulman, W. Baumeister, F. Wilfling, In situ cryo-electron tomogram of a bulk autophagy phagophore in S. cerevisiae #3. EMDB, https://www.ebi.ac.uk/emdb/EMD-15548. Accessed 8 September 2022.
76. A. Bieber et al., Tabular datasets for "In situ structural analysis reveals membrane shape transitions during autophagosome formation." Zenodo. https://zenodo.org/record/6607443. Deposited 2 June 2022.
77. A. Bieber, autophagy-tomo-analysis. GitHub. https://github.com/Anna-Bieber/autophagy-tomo-analysis. Deposited 15 June 2022.
78. A. Bieber, C. Capitanio, Anna-Bieber/autophagy-tomo-analysis: autophagy-tomo-analysis v1.0.0. Zenodo. https://zenodo.org/record/6607749. Deposited 2 June 2022.